ADVANCED FUNCTIONAL MATERIALS
www.afm-journal.de

Materials Views
www.MaterialsViews.com

In Situ Electrochemical Electron Microscopy Study of Oxygen Evolution Activity of Doped Manganite Perovskites

*Stephanie Raabe, Daniel Mierwaldt, Jim Ciston, Matthé Uijttewaal, Helge Stein, Jörg Hoffmann, Yimei Zhu, Peter Blöchl, and Christian Jooss**

Fundamental studies of catalysts based on manganese oxide compounds are of high interest since they offer the opportunity to study the role of variable valence state in the active state during O_2 evolution from H_2O. This paper presents a study of doping dependent O_2 evolution electrocatalysis of Pr-doped $CaMnO_3$ via in situ environmental transmission electron microscopy (ETEM) combined with ex situ cyclic voltammetry studies. ETEM studies of heterogeneous catalysis are a challenge, since the reactions in the H_2O vapor phase cannot directly be observed. It is shown that the oxidation of silane by free oxygen to solid SiO_{2-x} can be used to monitor catalytic oxygen evolution. Electron energy loss spectroscopy (EELS) as well as the in situ X-ray absorption study of near edge structures (XANES) in H_2O vapor reveals that the Mn valence is decreased in the active state. Careful TEM analysis of samples measured by ex situ cyclic voltammetry and an in situ bias-controlled ETEM study allows us to distinguish between self-formation during oxygen evolution and corrosion at the $Pr_{1-x}Ca_xMnO_3$-H_2O interface. Including density functional theory (DFT) calculations, trends in O_2 evolution activity and defect chemistry in the active state can be correlated to doping induced changes of the electronic band structure in A-site doped manganites.

1. Introduction

Oxygen evolution catalysis still represents the bottleneck for electro- or photo-chemical water splitting. Here, the outstanding problem is control of the multi-electron transfer reaction in oxygen evolution from water, which requires the transfer of four holes for the liberation of one molecule of oxygen. The hole transfer to H_2O and the intermediates formed during the oxidation process requires a minimum energy of $\Delta E^0 = 1.23$ eV per carrier (superscript 0 indicates thermodynamic equilibrium value at standard conditions if no other conditions are explicitly stated otherwise). The hole transfer can only be performed at low overpotentials if the catalyst can adjust the energy level of the donator states to the oxidation potential of H_2O and all subsequent transition states.[1] This requires a sufficiently complex atomic and electronic structure in the active state without suffering corrosive decomposition. The recent studies of structure and functionality of the $CaMn_4O_x$–based oxygen evolution center in natural photosynthesis[2–5] have provided insights into the pathway how nature solved the oxygen evolution challenge. The possibility that Mn-O compounds develop flexible mixed Mn valence states which strongly influence the Mn-O bonding strength and the charge transfer is believed to be crucial in the evolutionary selection of Mn sites for O_2 evolution.[7] Although there is agreement about this general picture, many details such as the detailed arrangement of mixed Mn valencies are not understood.[8]

Materials design of transition metal oxide catalysts relies heavily on the tailoring of electronic band structure and band occupation in the equilibrium state of the catalysts, in order to aim for optimum adjustments of the band edges to the oxidation potentials (see e.g.)[9–11]. Early mechanistic studies of perovskite oxides by Bockris and Otagawa suggested a correlation of catalytic activity with bonding strength between the B-site transition metal and oxygen due to occupation of antibonding d-states.[12] These trends have been recently reanalyzed by systematic DFT studies.[13–15] Based on the assumption that O_2 evolution from H_2O happens by a sequence of reaction intermediates $H_2O^* \rightarrow HO^* \rightarrow O^* \rightarrow HO_2^* \rightarrow O_2(g)$ (* indicates bonding of an O atom to the active B site), the main conclusion is that the B-O bonding strength represents a universal descriptor for the catalytic activity of O_2 evolution.[16] This confirms the trends

Prof. C. Jooss
Institute of Materials Physics
University of Goettingen
Friedrich-Hund-Platz 1, 37077 Goettingen, Germany
E-mail: jooss@ump.gwdg.de
S. Raabe, D. Mierwaldt, H. Stein, J. Hoffmann
Institute of Materials Physics
University of Goettingen
Friedrich-Hund-Platz 1, 37077 Goettingen, Germany
J. Ciston, Y. Zhu
Center for Functional Nanomaterials
Brookhaven National Laboratory
Upton, New York 11973, USA
J. Ciston
National Center for Electron Microscopy
Lawrence Berkeley National Laboratory
Berkeley, California, 94720, USA
Y. Zhu
Department of Condensed Matter Physics
Brookhaven National Laboratory
Upton, New York 11973, USA
M. Uijttewaal, P. Blöchl
Institute of Theoretical Physics
Technical University of Clausthal
Leibnizstr. 10, 38678 Clausthal-Zellerfeld, Germany

DOI: 10.1002/adfm.201103173

observed by Bockris and Otagawa that the activity increases from $LaCrO_3$ (d^3, strong O^* binding) over $LaMnO_3$ (d^4), $LaFeO_3$ (d^5), $LaCoO_3$ (d^6) to $LaNiO_3$ (d^7, weak O^* binding). A recent study by Suntivich et al.[17] demonstrates a volcano type relation between O_2 evolution activity and occupation of the antibonding Mn 3d e_g states for different B-site cations. This correlation differs from the one emphasized earlier, namely that between activity and the complete d-occupation on the Mn ion. Placing the focus specifically onto the occupation of the Mn e_g states can be rationalized via the larger hopping integral along the σ–antibond as compared to the π-bonding t_{2g} states. However, despite the significant progress in description of trends in the correlation between O_2 activity and electronic structure of complex oxides, many effects remain elusive. In particular, the effects of A-site doping on the band structure as well as the real non-equilibrium electronic and atomic structure in the active state are not well understood.

Based on their rich electronic phase diagrams and inspired by the role of flexible Mn valence in the natural oxygen evolution center, doped manganites $AMnO_3$ are particularly interesting model systems for fundamental studies of active states in O_2 evolution. A-site doping via heterovalent substitutions can tune the charge carrier concentration in the d-band between d^4 (Mn^{3+}) and d^3 (Mn^{4+}). For example, in $Pr_{1-x}Ca_xMnO_3$, $La_{1-x}Sr_xMnO_3$ and $La_{1-x}Ca_xMnO_3$, mixed Mn valence states can appear at intermediate doping[18] with a transition from overall p-doping at $x < 0.5$ to overall n-doping at $x > 0.5$. Due to electronic and electron-lattice correlation effects, doping can drastically alter the electronic band structure. Indeed, changes in A-site doping can induce transitions between phases with different band structure and magnetic properties sensitive to charge, orbital and polaron ordering.[19] At phase boundaries, such systems are very sensitive to external fields which can e.g. induce colossal resistance effects in electric fields.[20,21] Furthermore, studies of the active state must take into account the defect distribution and its evolution during the operation of the catalyst: Defects such as oxygen vacancies change the surface atomic structure and doping. They can thus affect the Mn-O-bond strength during activity but also may induce catalyst corrosion.

Here, we present an explorative electrochemical study combined with in-situ environmental TEM (ETEM) investigations of $Pr_{1-x}Ca_xMnO_3$ ($x = 0.0 - 1.0$) as a manganite model system for oxygen evolution catalysis with tunable Mn valence state. Our results give insight into the effects of A-site substitution and oxygen vacancy formation on the active state and the origin of electrode corrosion. High resolution ETEM based on aberration image C_S-correction is a relatively new method. High resolution imaging (e.g.[22]) and observation of change of particle shape in gas has been demonstrated,[23] but only a few studies were published on in-situ ETEM observations of catalytic processes.[24–26] The influence of the electron beam on the catalyst is not well understood. Inelastic scattering of electrons in the catalyst can induce atomic displacements (knock-on damage) as well as electronic excitations (electron-hole pairs, secondary electron emission). A well known consequence of secondary electron emission in semiconductors is the formation of a positive electric potential.[27] Combining different control experiments, in particular, application of an electric bias to the catalyst during in-situ ETEM experiments and during in-situ X-ray absorption near edge spectroscopy (XANES), we can develop insights into the effect of the electron beam on catalytic activity. Furthermore, we discuss the interplay between atomic and electronic changes in the active states and what controls the transition into corrosive decomposition of the catalyst.

2. Results

2.1. Voltammetry Study of Oxygen Evolution and Electrode Reduction

We have performed systematic cyclic voltammetry (CV) studies of oxygen evolution at $Pr_{1-x}Ca_xMnO_3$ (PCMO) thin film electrodes of different doping levels x. All CV studies are performed at 400 nm thick crystalline PCMO film electrodes on Pt/MgO with dominant [001] orientation. At all doping levels $0 \leq \times \leq 0.8$, oxygen evolution is observed for a positive potential above $E^0(H_2O \rightarrow 1/2\ O_2) = 0.82$ eV at pH = 7.

Figure 1 shows representative CV series measured at two different doping level x = 0.5 and x = 0.8, respectively. For x = 0.5, there is an additional reversible peak at $E^0 \approx 1$ eV (Figure 1a). The relatively small separation between the anodic and cathodic current peak, the strong sweep rate dependence as well as the weak dependence on the I-U-cycle number (see **Figure 2**) indicate a reversible surface oxidation/reduction. As also confirmed by TEM inspection, the electrode is entirely stable at U = 1.43 V vers. SHE over a period of 90 min (see supporting information Figure S2). In contrary, at x = 0.8, an irreversible process centered at about +0.35 eV is observed (Figure 1b). It is associated with high cathodic and even higher anodic current densities. Peak areas and separation significantly increase with cycle number and thus clearly outweighing the sweep rate dependency. This indicates fast electrode corrosion related to diffusion controlled phase transition. The chemical analysis of corroded electrodes by energy-dispersive X-ray spectroscopy (EDX) reveals an A-site dissolution at the electrode surface which manifests in the formation of an amorphous MnO_x surface (see supporting information Figure S2d).

The exchange current density for oxygen evolution at thin film electrodes is of the order of a few nA/cm² and shows a doping dependence with a maximum of $j_0 \sim 11$ nA/cm² at x = 0.32 (Figure 2a). The overpotential η required for O_2 evolution approximately agree to the values observed by other authors.[12,17] For A-site doping, the overpotential η exhibits a significant decrease from x = 0 to x = 0.32 and no significant trend for higher doping (Figure 2b). The substitution x of Pr^{3+} by Ca^{2+} can be translated into a Mn 3d e_g occupation which is presented in Figures 2a and b as well and will be discussed in Section 3. For further details of electrochemical analysis, see supporting information, i.e., Figures S1, S2 and S3.

2.2. In-Situ Study of Activity via Environmental TEM

ETEM observation of catalytic activity of a material which catalyzes reactions in the gas phase is difficult, because small changes of the chemical composition of the gas must be

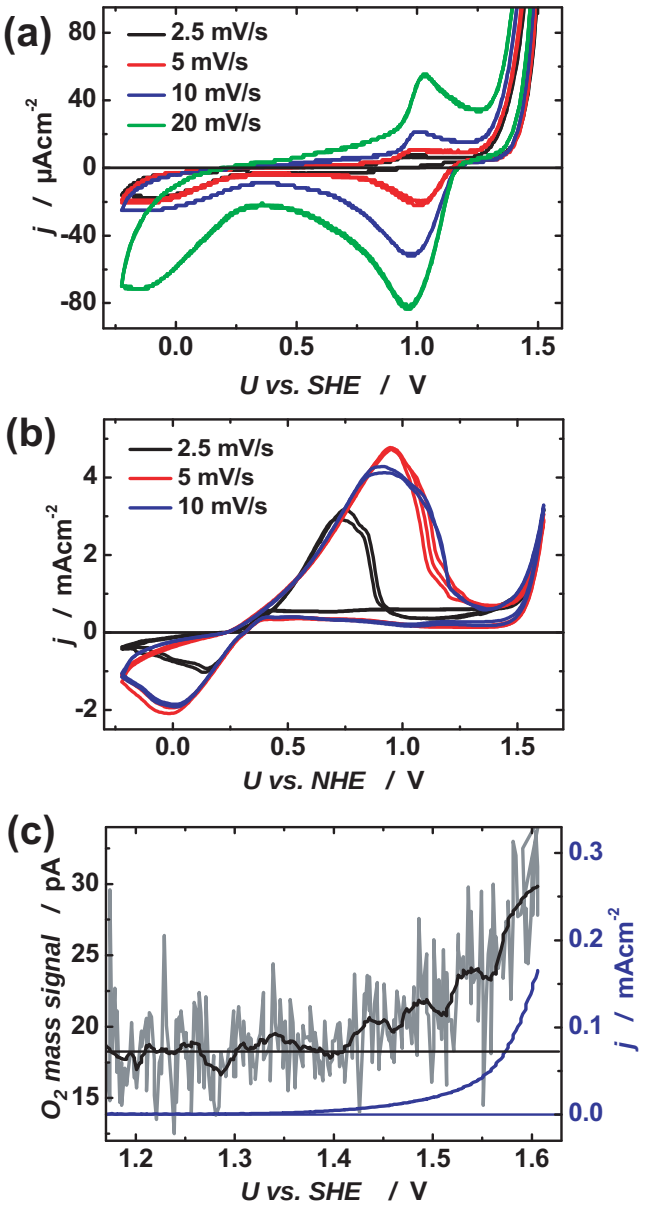

Figure 1. Cyclic voltammetry (CV) of single-crystalline $Pr_{1-x}Ca_xMnO_3$ thin films. (a) Current density (*j*)–potential (*U*) curves for x = 0.5 and sweep rates from 2.5 mV/s to 20 mV/s. (b) CV for x = 0.8, cycles 8-9 at 10mV/s, cycles 11-12 at 2.5 mV/s, cycles 19-21 at 5 mV/s (c) Correlation between *j*–*U* curve and O_2 mass signal at 2 mV/s for x = 0.5.

monitored by mass spectroscopy. We found that the O_2 evolution can be monitored in the presence of small amounts of SiH_4 to the H_2O/He gas mixture. During oxygen production, SiH_4 is consumed and solid SiO_{2-x} grows on top of the active crystalline surface of the catalyst. As will be evidenced in detail in the following paragraphs, we find that electron beam induced SiO_{2-x} formation at crystalline PCMO edges in contact with SiH_4/H_2O vapor is due to electrocatalytic O_2 evolution, where the required positive potential develops due to secondary electron emission. Thus, the growth rate of the SiO_{2-x} layer is a direct measure of catalytic activity for O_2 evolution.

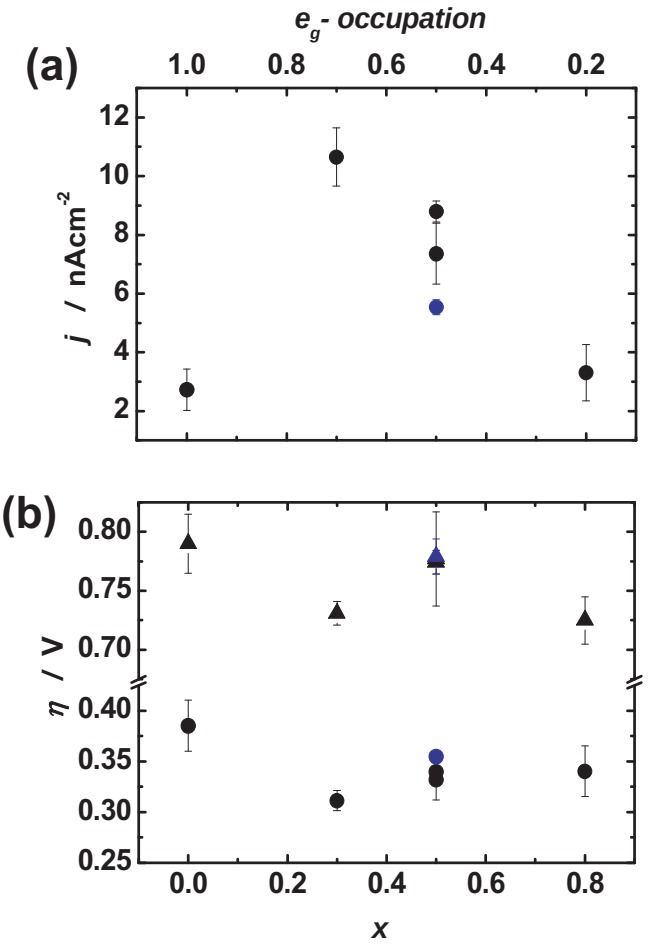

Figure 2. (a) Exchange current density for oxygen evolution and (b) overpotential η for j = 1 µA/cm^2 (circles) and j = 930 µA/cm^2 (triangles) of PCMO thin film electrodes as a function of doping x. Black symbols represent data of the second *I*-*U*-cycle while blue symbols show data of the seventh *I*-*U*-cycle.

In high vacuum, PCMO ($0 \le x \le 1$) is fully stable against beam damage in electron fluxes of more than 10^6 e/(Å^2 s). **Figure 3**a reveals a high-resolution TEM image of a crystalline PCMO (x = 0.32) sample edge before injection of H_2O vapor at [001] zone axis. PCMO has space group Pbnm over the entire doping range which corresponds to the charge disordered phase and has been confirmed by electron diffraction. In some thin areas near the edge to the vacuum, the sample reveals a 2 × 2 superstructure, which provides evidence for an oxygen deficiency and a related oxygen vacancy ordering.

After injecting the H_2O/He mixture with H_2O partial pressure of ~ 0.013 mbar into the sample chamber, the sample is equilibrated for 30 min in the gas without electron exposure to account for thermal drift induced by convective cooling. Electron beam illumination of a crystalline PCMO sample area with 10^4 e/(Å^2 s) induces immediate growth of an amorphous SiO_{2-x} layer at crystalline edges (Figure 3b,c, see movie M1 in the supporting material). Simultaneously, the 2 × 2 superstructure gets more pronounced and is extended over a much wider area. The thickness of the SiO_{2-x} layer rapidly increases within minutes to

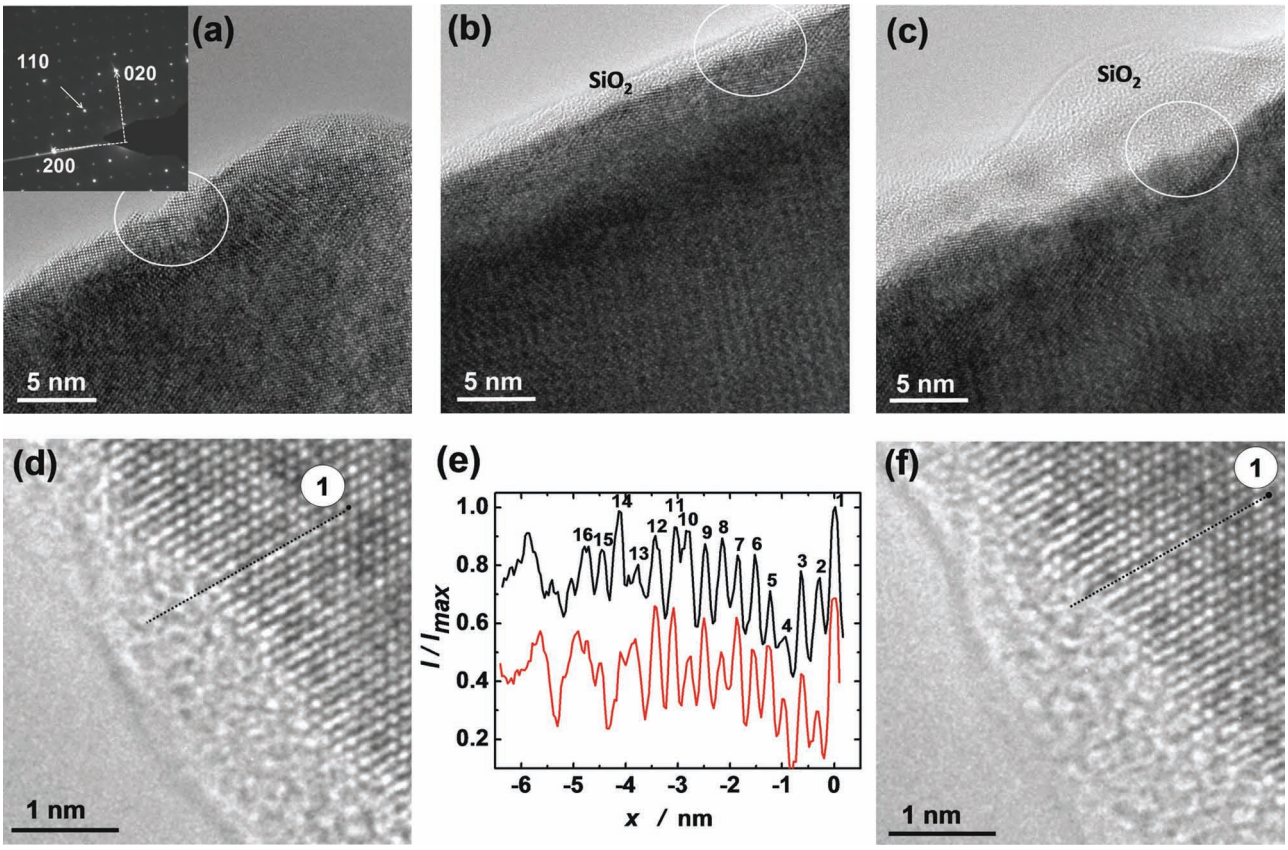

Figure 3. ETEM study of crystalline PCMO x = 0.32 during electron and water exposure. (a) High-resolution bright field TEM image acquired in high vacuum showing the pristine state of a grain at [001] zone axis with the crystalline area fully extended to the edge. The inset shows a electron diffraction pattern of the same area near [001] zone axis showing Pbnm Bragg reflections with a 2 × 2 superstructure. The same section as in (a) is shown during an ETEM experiment in water vapor, where the growth of an amorphous SiO_{2-x} layer indicates oxygen evolution activity of the edge (b) 20 s and (c) 70 s after start of the electron beam stimulation. The grey circle is a marker for a specific edge location. (d–f) Interplay between catalysis and corrosion at another area of the same sample. (d) and (f) High-resolution TEM images of a grain at [201] zone axis after 300 s and 310 s of electron beam exposure in water vapor and resulting SiO_{2-x} coverage. (e) Intensity modulation along the same line depicted in (d) and (f). The first atomic column of this line is labeled as "1". The distance between atomic columns along the lines corresponds roughly to half of the b lattice constant (0.285 nm). The change from a periodical to a more or less statistical oscillation indicates the crossover from well-crystalline PCMO to corroded amorphous PCMO followed by SiO_{2-x}, respectively.

several nanometers (Figure 3b-c). Above a thickness of ~ 10 nm, the growth rate drastically slows down. A subsequent analysis of this layer by electron energy loss spectroscopy (EELS) as well as by EDX clearly indicates that the layer consists of SiO_{2-x} formed by oxidation of gaseous SiH_4. The SiO_{2-x} growth is observed all over the electron irradiated crystalline PCMO regions including the top and bottom surfaces. However, the spatial distribution within the irradiated region is inhomogeneous most likely due to surface topology and its impact on the SiO_{2-x} nucleation.

The SiO_{2-x} formation can entirely be suppressed by reducing the electron exposure below 10^3 e/(Å^2 s) and was neither observed by illumination of the Cu grid nor at amorphous PCMO edges for any intensity of illumination. A control experiment at an amorphous edge of the same grain as shown in Figure 3 is presented in the supporting information (Figure S4). Therefore, oxidation of SiH_4 takes place only on top of regions with crystalline PCMO, while regions with amorphous PCMO remain inert. This rules out that SiH_4 is directly oxidized by a direct reaction with H_2O vapor and suggests that SiO_{2-x} growth can be used as an indicator for local O_2 evolution activity of the catalyst material (see also supporting information Figure S8).

In its active state during O_2 evolution, PCMO undergoes structural and electronic changes which have been studied via EELS in the ETEM and via in-situ XANES in water vapor (see **Figure 4**). Changes in electronic structure are visible in the Mn core loss spectra which are acquired by EELS at distances between 3 nm and 30 nm from the interface to SiO_{2-x}. The peak ratio of the Mn-L_3 and Mn-L_2 lines is used to calculate the Mn valence (see supporting information for details). In the ETEM experiment (Figure 4a), the L_3/L_2 peak ratio increases from the virgin state in high vacuum to the state measured directly after performing active O_2 evolution in H_2O vapor and switching back to high vacuum mode. The increase of the L_3/L_2 peak ratio is measured all over the electron-beam exposed area and indicates a reduction of the Mn mean valence from +3.2 ± 0.7 (virgin state) to values around +2.0 ± 0.9 (post mortem analysis

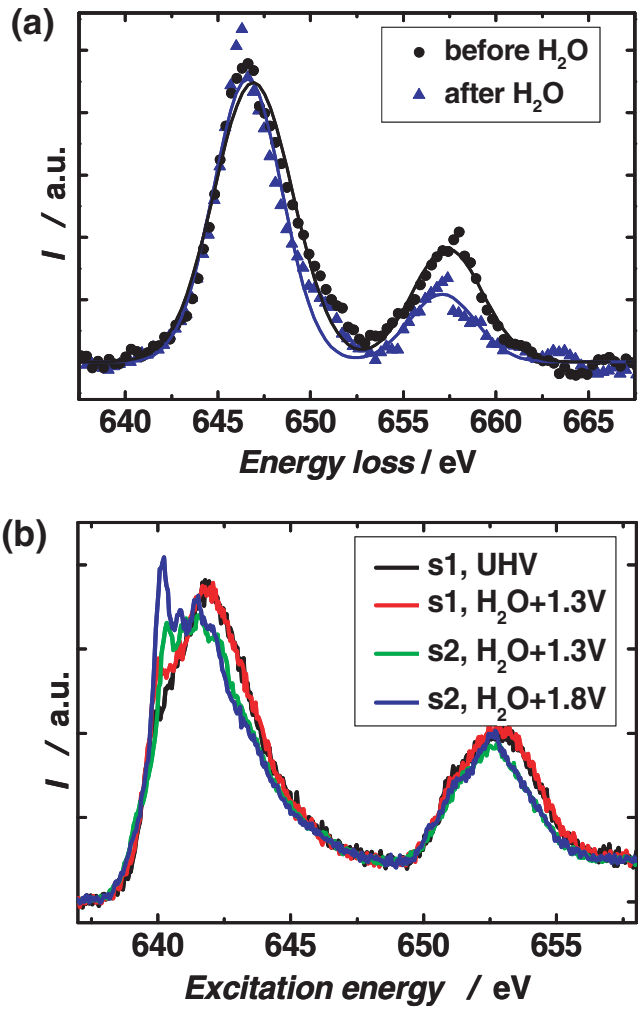

Figure 4. Change of the Mn L-edges in the active state of PCMO x = 0.32 revealed by in-situ ETEM (a) and in-situ XANES (b) experiments. (a) Core loss EELS spectra after Hartee-Slater background subtraction before and after electrocatalytic O_2 evolution. Both spectra are acquired in high vacuum mode before switching to and after switching back from ETEM operation mode and stimulating the sample in 0.013 mbar H_2O vapor with 10^4 e/Å^{2}s. The L_3/L_2 ratio increases from 2.5 to 4.8. (b) In-situ XANES study of two PCMO films s1 and s2 with x = 0.32 in UHV and in contact with H_2O vapor at different positive bias. The increase of intensity at the L_3 edges at about 640.3 eV indicates an increasing fraction of Mn^{2+}.[43]

of active state). The measured Mn valence in the virgin state corresponds to the valence of +3.3 which is expected from the hole doping at x = 0.32.

A mean valence close to 2+ without changes in the cation composition corresponds to the formation of Mn^{2+} in electron-doped $Pr_{0.68}Ca_{0.32}MnO_{3-\delta}$ with $\delta \approx 0.5$ during catalytic activity. The transition to the Brownmillerite phase via progressive oxygen vacancy creation and ordering in the major part of the stimulated area is also supported by increase of area with 2×2 superstructure. In order to rule out that oxygen vacancy formation is mainly due to the effect of high energy electrons in the ETEM, XANES measurements of the change of the Mn L_3/L_2 edges of PCMO films (x = 0.32) in contact with H_2O vapor were performed. In addition, the change of the Mn L-edge in contact with H_2O vapor and under application of a positive bias is monitored (Figure 4b). The shift from 641.9 eV to a lower excitation energy of 640.3 eV confirms the decrease of Mn valence state through an increase of the fraction of the Mn^{2+} species. Although the excitation conditions are very different, the same trend in Mn valence change is observed via both in-situ methods, where the electrodes are in contact with H_2O vapor. It is most likely that the observed Mn valence decrease is an intrinsic feature of the active state of PCMO at x = 0.32. The formed phase which is similar to oxygen deficient Brownmillerite is quite stable in the active state and can be well separated from corrosion process.

2.3. In-Situ Study of Catalyst Corrosion Via Environmental TEM

The combination of electron beam exposure at 10^4 e/(Å^2 s) and water environment causes corrosive degradation of PCMO at the interface to SiO_{2-x} which is rather slow for x = 0.32 and fast for x ≥ 0.75. Dynamic observations are shown in the supporting information (movies M2 for x = 0.32 and M3 for x = 0.95). Analyzing the time evolution of a row of atomic columns (Figure 3d–f), the periodic oscillations which indicates well-crystalline PCMO (x = 0.32) are reduced by two atomic columns in 10 s via amorphization. Notably, the growth of the SiO_{2-x} layer is ~10 nm/min, much higher than the interface recession of ~1.8 nm/min. The ratio of the rates of SiO_{2-x} formation to PCMO degradation indicates catalytic turnover numbers of about 10 under the specified ETEM conditions. Thus, reduction of the PCMO (x = 0.32) is not a main source of oxygen for SiO_{2-x} formation.

In strong contrast, non-doped $PrMnO_3$ and PCMO electrodes with high Ca concentration (x = 0.8, 0.95 and 1) undergo drastic corrosion processes in ETEM experiments at the same H_2O partial pressure and electron flux. As a typical example, **Figure 5** shows the results for x = 0.95. Crystalline edges remain completely stable under electron irradiation of more than 10^6 e/(Å^2 s) in high vacuum (Figure 5a). Exposure to water with partial pressure of ~ 0.013 mbar under an electron flux of 10^4 e/(Å^2 s) causes first re-crystallization toward an intermediate phase with a crystal symmetry incompatible with perovskite structure and subsequently a transition to a nearly amorphous phase with some nanocrystalline grains (Figure 5b,c). The diffraction spots originating from the recrystallized phase are significantly broadened compared to the sharp reflections of the initial crystal phase (Figure 5d,e). This broadening may be interpreted in terms of an initiating chemical decomposition. This is confirmed by the contrast variations within the recrystallized domain in the annular dark field STEM image in Figure 5c. It is acquired at a scattering angle of 35–70 mrad and is thus a mixture of diffraction contrast and Z contrast. Local EELS analysis of corroded recrystallized as well as amorphous regions shows presence of Pr, Ca, Mn and O, but the Ca/Mn ratio is decreased by 30–40% after water exposure. This indicates a substantial A-site depletion and decomposition of Ca-rich compounds in water vapor. In the early stages of the electron-beam driven reaction, small nuclei of SiO_{2-x} start to grow but quickly disappear during the progression of the corrosion

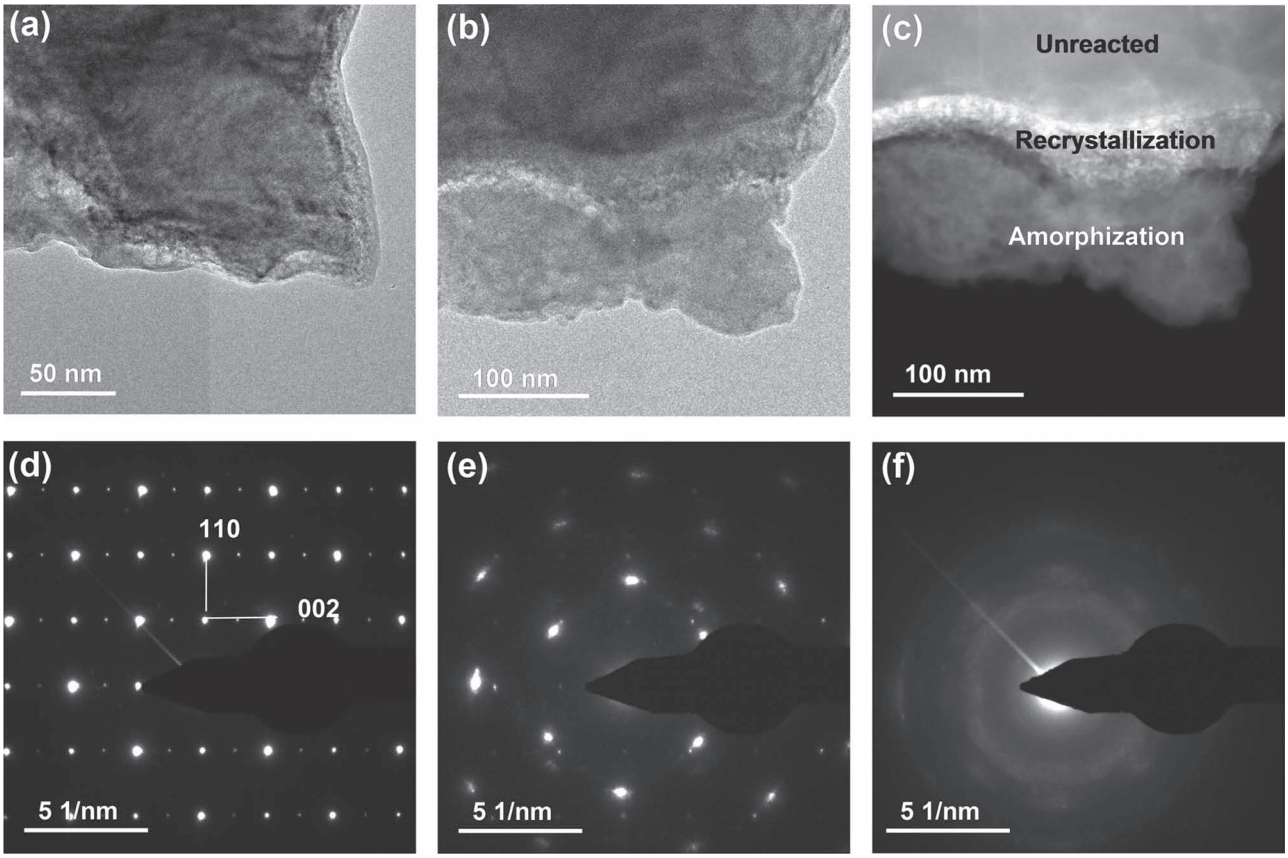

Figure 5. Corrosive behavior of PCMO x = 0.95 bulk exposed to H_2O vapor during stimulation with 300 kV electrons. (a) Bright field TEM image before gas injection shows a crystalline sample edge in the [-110] zone axis. The corresponding diffraction image (d) reveals Pbnm structure. Bright field TEM image (b) and annular dark field STEM image (35-70 mrad collection angle) (c) of the same area after exposure with 2 min electron flux of $10^4 e/Å^2 s$ in 0.013 mbar H_2O. A pronounced corrosion due to recrystallization and subsequent amorphization is observed. Unreacted and amorphous regions are separated by recrystallized domains. Only one small nucleus of SiO_{2-x} is observed (white circle). (e) The diffraction pattern of the recrystallized domains reveals a crystal symmetry inconsistent with the initial Pbnm symmetry and is most likely Mn rich cubic phase. The observation that the recrystallized region exhibits a unique crystal orientation and symmetry with broadened peaks combined with the strong inhomogeneity of contrast in the STEM images indicates an initiating chemical decomposition. (f) The diffraction pattern of the amorphous regions.

process. With a rate of ~ 80 nm/min, the corrosion front in the x = 0.95 samples moves 80 times faster than for x = 0.32 and no catalytic turnover is obtained.

2.4. Bias Control of Processes Via an Electrochemical Cell

Our hypothesis that an electron beam induced positive electric potential due to secondary electron emission drives the electrocatalytic activity of PCMO as well as the corrosive degradation can be directly proven by application of an electric bias to the PCMO electrode. In order to perform this electrochemical ETEM experiment under well controlled conditions, we have used a TEM sample holder with a piezo-controlled nanotip, where an electric potential can be applied to the TEM sample (**Figure 6**). The so formed electrochemical cell is composed of a PCMO working electrode (x = 0.95), a Pt/Ir tip as counter electrode and the $He/H_2O/SiH_4$ gas mixture as an analogue to an electrolyte. In order to minimize the resistance between both electrodes, the tip is carefully set into contact with the working electrode (Figure 6a,b). At a negative voltage of about –1 V, neither SiO_{2-x} formation nor corrosive recrystallization/amorphization processes are observed (Figure 6c,d) although the same electron flux was applied for stimulation as in Figure 5. As confirmed by electron diffraction (Figure 6d), the Pbnm crystal structure remains entirely intact. The observed change in the shape of the electrode during the ETEM experiment at –1 V is due to mechanical contact forces between the tip and the sample.

3. Discussion

3.1. Band Structure Trends in O_2 Evolution Activity

Understanding catalytic O_2 evolution requires detailed understanding of the strengths of Mn-O and O-O bonding at the surface as well as of the charge transfer processes of hole carriers between the electrode surface and the adatoms. The full theoretical description of such processes including surface

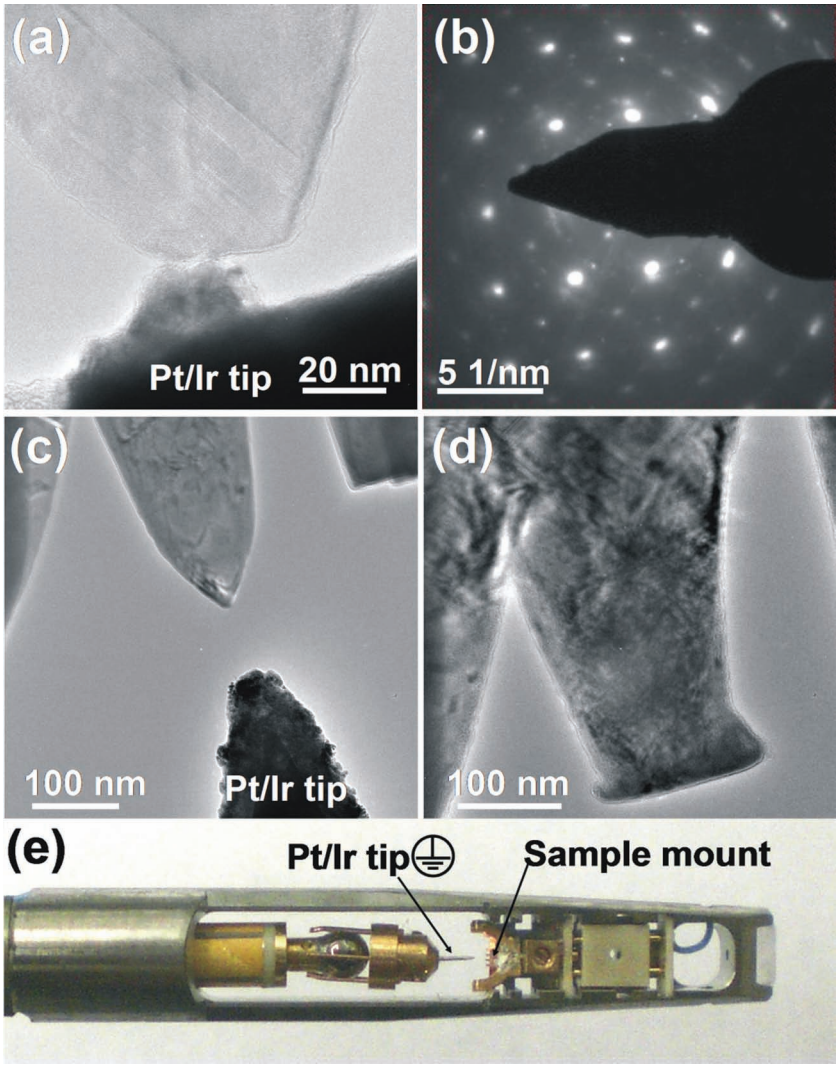

Figure 6. Two electrode electrochemical cell in the ETEM with PCMO x = 0.95 working electrode and Pt/Ir as a counter electrode. (a) Bright field overview TEM image shows the two electrode configuration with a well-crystalline PCMO (x = 0.95) grain at [001] zone axis in the virgin state just before and (b) during contact with the PtIr tip. (c) Bright field image of the same grain after H2O and electron expose with applied bias of -1V. The absence of SiO2-x growth indicates that oxygen evolution is suppressed at negative bias. (d) Diffraction pattern after reaction in gas. Neither recrystallization nor amorphization is observed and the perovskite structure of the electrode remains entirely intact. (e) Sample holder with piezo-controlled nanotip which is used to set up the electrochemical cell (see section 5).

states in the active state of the catalyst is far beyond the scope of this work. We focus here on the effect of A-site doping on the bulk band structure of PCMO in order to discuss the observed doping trends. The main features are schematically shown in **Figure 7** taken into account experimental data as well as DFT calculations (for details see supporting information, Figures S5 and S6).

$CaMnO_3$ is a charge-transfer insulator, i.e. the valence band top is made from O-2p states, while the conduction band is dominated by Mn d e_g states.[28–30] In contrast, $PrMnO_3$ resembles a Mott insulator, where however, the band gap is between the lower and upper Mn 3d $e_{g\uparrow 1}$ and Mn 3d $e_{g\uparrow 2}$ bands which are split by a static cooperative Jahn-Teller effect. Therefore, the upper valence band edge and the lower edge of the conduction band are both dominated by anti-bonding Mn 3d $e_{g\uparrow}$ states.

If a rigid band approximation applies for different doping levels the substitution of Pr^{3+} by Ca^{2+} leads to hole doping of the lower e_g-band in $Pr_{1-x}Ca_xMnO_3$ visible in a shift of the work function φ. However, the available data for φ in PCMO in the doping range $0 \leq x \leq 1$ (see supporting information S6) show a small drop between x = 0 and x = 0.3 which reflects the disappearance of the band gap for $0.3 \leq x \leq 0.7$ at room temperature.[31] In this doping range, a low-temperature charge/polaron ordered phase is present, where the lower e_g band is further divided. In the charge ordered state, the opening of a gap of 0.25 (x = 0.3) to 0.15 (x = 0.5) eV is observed.[32] The nearly constant φ value up to x = 1 indicates a reorganization of the top valence band edge with an increasing weight of O 2p states which ends in the establishment of an charge transfer insulator at x = 1.

Our study of the trends in catalytic O_2 evolution activity as a function of A-site doping show interesting correlations to specific changes in the electronic band structure. We observe an increase of the exchange current density and decrease of the overpotential for increasing e_g occupation (Figure 2) with the exception of x = 0 which requires much larger overpotentials. It is shown for several perovskite oxides in the study of Suntivich et al.[17] that Mn 3d e_g occupation is a good descriptor for the Mn-O bonding strength which determines the left side of the volcano.[13] Except for x = 0, the trend in our data agrees with this statement (see supporting information S7). In this doping range ($0.3 \leq x \leq 0.8$), a "metal-like" Mn 3d e_g-O 2p conduction band is formed at the Fermi level and its occupation can be continuously changed with x. In contrast, for undoped $PrMnO_3$ with the highest nominal e_g filling, the e_g band is split due to a cooperative Jahn-Teller effect and orbital ordering (Figure 7). The splitting significantly reduces the energy of the occupied Mn 3d $e_{g\uparrow 1}$ states. Such strong changes in the band structure indicate that a picture, where the strength of the Mn-O bond simply depends on the occupation of an otherwise rigid e_g band has serious limitations when correlation effects become important.

Most favorable electrocatalytic properties are observed for p-doped PCMO in a doping range $0.3 \leq x \leq 0.5$, where hole carriers are polarons with relatively high mobility and have mixed Mn 3d e_g and O 2p character. From the highest j_0 in that doping range, we conclude that such mobile hole states in more or less covalent Mn-O bonds can establish the most efficient charge transfer across the PCMO-H_2O interface.

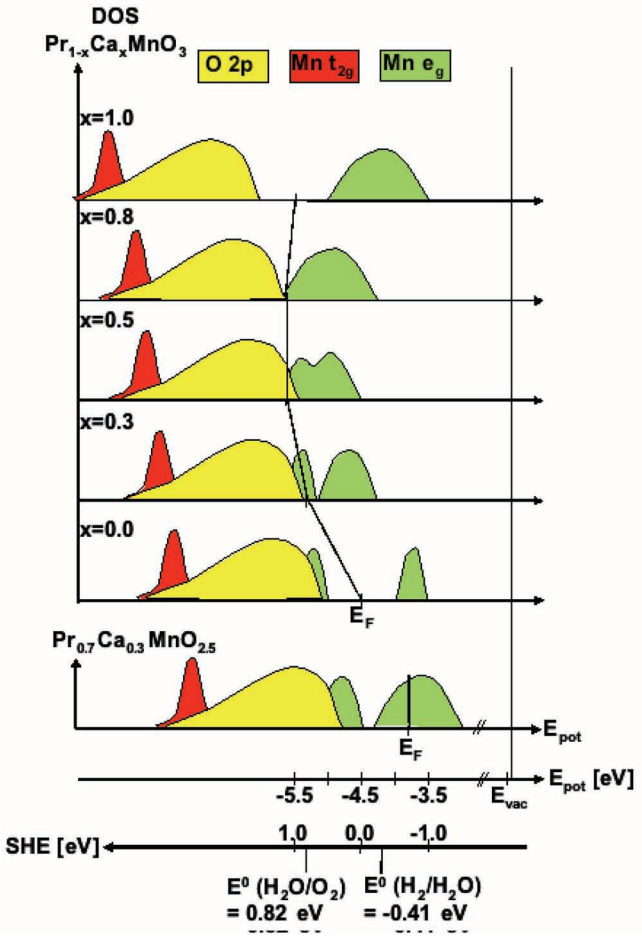

Figure 7. Schematic evolution of the band structure of $Pr_{1-x}Ca_xMnO_3$ based on DFT calculations and literature results (see supporting information Fig. S5 and Fig. S6). The schematic representation mainly focuses on change in the work function (Fermi level), the splitting and shifts of the Mn 3d e_g majority states due to the Jahn-Teller effect, the shift in the O2p states and the resulting overlap of Mn 3d and O 2p states. The energy scale is shown with respect to the vacuum level and to the electrochemical SHE. Potentials E^0 for oxygen and hydrogen evolution at pH = 7 are also indicated.

3.2. Electron Beam Driven O_2 Evolution Catalysis in the ETEM

The two major excitation effects of 300 keV electron beam are related to inelastic scattering at atomic nuclei and electrons. The former can generate element specific atomic displacements (knock-on damage) above a critical acceleration voltage and above a critical electron flux (see e.g.)[33]. The latter can generate electronic excitations such as electron-hole generation and secondary electron emission. Emission of secondary electrons can leave holes behind them. Depending on the mobility of charge carriers in the material secondary electron emission thus can generate a positively charged area at samples with potential up to several 10 V.[27] For PCMO under an electron flux of 10^4 e/(Å^2 s), we estimate a potential of the order of ~ 1 V, a value which is also evidenced by the observation that electrochemical activity can be fully suppressed by a negative bias of 1 V. A quantitative modeling of the induced positive space charge layer is beyond the scope of this paper and will be published elsewhere.[34] Depending on the exact value of the oxidation potential $E(H_2O \rightarrow O_2)$ under ETEM conditions, the beam induced positive potential is thus able to shift hole states to a positive overpotential and thus drive the electro-catalytic O_2 evolution.

Electron beam driven SiO_2 growth represents a direct solid-state indicator for electrocatalytic activity of crystalline PCMO edges. Under ETEM conditions, the SiH_4 oxidation is correlated to electrocatalytic oxygen evolution at PCMO electrodes using the H_2O/He/SiH_4 gas mixture as an electrolyte. Direct SiH_4 oxidation either via deoxygenation of PCMO or via reaction of H_2O can be directly excluded since SiO_{2-x} growth does not happen under electron beam stimulation if PCMO corrosion becomes significant or at an inactive PCMO edge (e.g. amorphous areas due to TEM sample preparation). The electrocatalytic O_2 evolution is also visible by the increase of the O, O_2 and H_2 mass signals when the electron beam is shifted from vacuum to a catalytic active sample edge (see supporting information S8).

3.3. The Active State of the Catalyst

Oxygen vacancies at oxide catalyst surfaces often play an important role for catalytic activity (see e.g.)[13], since they influence coordination, bonding strength, doping and electronic states at the surface. Our observation of Mn valence decrease during oxygen evolution activity (ETEM) and under similar conditions in in-situ XANES gives direct evidence that oxygen vacancies (V_O") are formed during oxygen evolution activity. The observation of Mn^{2+} in ETEM correlates with pronounced 2 × 2 superstructures which are typically observed in oxygen deficient manganites.[35]

CV measurements show the presence of a reversible redox process at the surface of PCMO electrodes in the doping range $0.3 \leq x \leq 0.5$ near $E^0(Mn^{4+}/Mn^{2+}) \approx 0.76$ eV vers. SHE[36] at pH = 7. By taking into account our in-situ observations of the Mn L edges, this indicates a near surface vacancy formation process according to $Pr_{1-x}Ca_xMn^{3+x}O_3 + 2e \leftrightarrow Pr_{1-x}Ca_xMn^{2+x}O_{2.5} + V_O" + ½\ O_2$ at a redox potential of $E^0{}_P\ (Mn^{4+}/Mn^{2+}) \approx 1$ V vers. SHE. Compared to E^0 for MnO_2/MnO this is slightly enhanced due to the increased stability of the perovskite structure.[37] The observed initial decrease of the current density in chronoamperometry measurement at U = 1.43 V vers. SHE (supporting information Figure S2) by a factor of 3 can possibly be attributed to surface oxygen vacancy formation. Since the creation of oxygen vacancies leads to doping by two electrons per vacancy, a significant decrease of the work function is expected by incorporation of oxygen vacancies. Indeed, Beyreuther et al. observe a decrease of φ by 1 – 1.7 eV in $La_{0.7}Ca_{0.3}MnO_{3-\delta}$ and $La_{0.7}Ce_{0.3}MnO_{3-\delta}$ for $\delta \approx 0.5$–0.7.[38] Because oxygen vacancies represent electron donors, their formation energy increases with the energy difference between the upper edge of the O2p band and the Fermi level

The presence of a band gap, such as for $CaMnO_3$, therefore hamper the oxygen vacancy formation and may facilitate phase separation into Ca-rich and Mn-rich phases with a subsequent

corrosive decomposition of the oxide. In contrast, the "metal like" valence band at intermediate doping can be continuously filled up with electrons. The resulting increase of E_F may slow down the electrode reduction and facilitate O_2 evolution activity by an increasing Mn 3d e_g occupation (Figure 7 lower panel).

Although under ETEM conditions, the determination of equilibrium potentials for a redox reaction measured versus a reference electrode is not possible, our experiments show similar trends in ex-situ and in-situ experiments. We therefore suggest that both the formation of oxygen deficient phases as well as oxygen evolution from water splitting can be driven by the positive overpotential η which develops under electron beam stimulation.

3.4. Corrosion Phenomena

Many perovskites are only stable during water splitting in alkaline media. Under electrochemical stimulation at pH = 7 oxygen evolution via water splitting can be counteracted by corrosive phase changes. Parallel trends are observed in CV and ETEM experiments, showing pronounced corrosion in Ca rich samples. In the CV and chronoamperometry experiments, we observe dissolution of Pr/Ca cations in the electrolyte after cycling to sufficiently negative potential with respect to $E^0_p(Mn^{2+}/Mn^{4+})$. A-site cation dissolution and electrode corrosion is typically observed for other perovskites in a range of $E^0(LaBO_3/La^{3+}) \approx 0.2–0.35$ eV vers. SHE.[39] The presence of a MnO_x surface layer at the corroded electrodes (see supporting information Figure S2d) suggests a reaction according to $AMnO_3 + 3H_2O \leftrightarrow A^{n+}(aq) + MnO_{2-y} + (1 + y/2)O_2 + 2H_3O^+ + 2e$ as a typical corrosion reaction for perovskites in acidic aqueous solution.

In the ETEM studies, we observe by EELS analysis that degradation via recrystallization and amorphization in Ca-rich samples is accompanied by a Ca depletion of the reacted zones. The diffraction patterns of the Ca-depleted recrystallized areas are compatible with a cubic Ca-Mn-O phase which is subsequently transformed into MnO rich amorphous areas. This resembles the formation of Mn oxide in the ex-situ voltammetry experiments due to A-site cation dissolution in the electrolyte. The suppression of the corrosion reaction via a negative potential in the in-situ ETEM experiment directly rules out that knock-on damage is the main driving force for corrosion and gives strong evidence for the presence of electrochemically driven corrosion.

Corrosive behavior is increased for Ca-rich manganites due to reduced phase stability. Indeed, the formation enthalpy of A-site doped manganites decreases with increasing Mn valence.[40] Undoped $CaMnO_3$ has only a very narrow stability range in the pseudobinary CaO-MnO phase diagram and can easily decompose into Ca- rich and Mn-rich phases.[41] The decomposition kinetics can be strongly influenced by the defect chemistry of the catalyst in its active state: Because oxygen vacancy formation may be less favorable in the single phase $CaMnO_3$ pervoskite with a band gap, it can easily drive the phase decomposition and thus may play an important role in the catalyst corrosion.

4. Conclusions

Although manganites exhibit relatively large overpotentials for electro-catalytic O_2 evolution (e.g. in comparison to RuO_2), they represent interesting model systems for the study of the role of e_g doping, covalence and defect chemistry on catalytic activity. In particular, we observe that near surface oxygen vacancies are formed in neutral conditions (pH = 7) which decrease the Mn valence and thus increase the e_g occupation. This may be essential for the observed reduced oxygen evolution activity compared to expectations of activity based on the equilibrium e_g doping level. First steps in understanding electron beam driven electrochemical processes in an ETEM are demonstrated, where we observe oxygen evolution activity as well as corrosive decomposition. The suppression of O_2 evolution as well as corrosive processes via a negative potential in the in-situ ETEM electrochemical cell, directly rules out that knock-on damage is the main driving force for corrosion and supports our conclusions that catalysis as well as corrosion is driven by a positive electrical potential. We find that subtle band structure effects such as the splitting of the Mn 3d e_g states and changes in the character of the hole states have an impact on charge transfer during water oxidation and may decide whether oxygen vacancy formation is assisting catalysis or corrosion. Our findings may stimulate more detailed and atomic level studies on the role of oxygen vacancies for catalytic activity in perovskites. We expect that strategies which can stabilize non-equilibrium concentrations of defects in the active state of the catalyst and can thereby improve the catalytic activity without corrosion are of high importance for the future optimization of catalyst materials.

5. Experimental Section

Sample Preparation: Bulk $Pr_{1-x}Ca_xMnO_3$ samples (x = 0.32, 0.8, 0.95, 1.0) were prepared via a grinding and sintering process starting from a stoichiometric mixture of dry Pr_6O_{11}, $CaCO_3$, and Mn_2O_3 powder. After repeated milling in a ball mill and calcination in air, cold-pressing and closing sintering at 1370 K for 48h, the polycrystalline samples reveal only the orthorhombic phase (space group: Pbnm) with a small amount of the charge-ordered $P2_1nm$ PCMO for x = 0.32 but no secondary phases. From the bulk sample electron-transparent specimens were prepared by a polishing and dimpling process and a final single-sided Ar ion etching at 3 kV at an angle of 12°. The sample used for electrochemical TEM (Figure 6) was cut via focused-ion-beam (FIB) in a FEI Nova Nanolab 600 using Ga ions with energies ranging from 30keV and 7nA (initial cuts) to 5keV and 29pA (final Ga-milling). Finally, Ar ion etching at 3 kV at an angle of 12° is performed in order to minimize the amount of FIB-damages sample volume. Depending on the position, grains with diameter of several 100 nm can reveal well-crystalline edges as well as amorphous edges. This indicates that irradiation damage like oxygen vacancies cannot be completely excluded. The samples were glued either on a copper grid or on a tantalum ring and electrically grounded to minimize electric charging effects.

$Pr_{1-x}Ca_xMnO_3$ thin films (x = 0-0.8) for CV studies were deposited by ion-beam-sputtering at a deposition temperature of T_{dep} = 795 °C and an oxygen partial pressure of $P_{O2} = 10^{-4}$ mbar. 400 nm thick PCMO films with different Ca contents were deposited on almost single-crystalline Pt templates on [100] MgO, in order to obtain a conducting back-contact. The PCMO films are predominantly [001] orientated but typically twinned, leading to a [110]-orientated volume fraction. [111] misorientations in the Pt give rise to a volume fraction of [112] grains in the PCMO. Inspection

of the PCMO films via optical and scanning electron microscopy shows complete coverage of the template without any holes or cracks. Undoped $CaMnO_3$ films (x = 1) have been excluded from this study because they have not been successfully prepared as single phase material.

In-situ ETEM experiments and electron loss spectroscopy: A C_s image-corrected FEI Titan 80 – 300 kV electron microscope with a point resolution of 0.08 nm including a differentially pumped environmental cell is used for electron diffraction, high-resolution imaging and electron energy loss spectroscopy (EELS). The base pressure without gas injection is 10^{-6} mbar. Water injection is performed by inlet of He gas bubbled through distilled water. The total pressure during exposure amounts to 1.3 mbar with an estimated H_2O partial pressure of 0.013 mbar. In order to study chemical reactions at catalyst-vapor interfaces, a gaseous sacrificial Si-containing compound is used. In preliminary experiments, we observed that SiH_4 is present as an impurity in the sample chamber. The correlation between silane oxidation to solid amorphous SiO_x by sufficient amounts of evolving oxygen at crystalline catalyst surfaces is used for systematic studies of the catalytic water splitting activity in a series of 8 PCMO samples with different doping levels (x = 0, 0.32, 0.8, 0.95 and 1). High-resolution bright field imaging is performed on PCMO grains orientated to a low index zone axis.

A Gatan Tridiem energy filter for Electron Energy Loss Spectroscopy (EELS) and elemental mapping is installed. For high spatial resolution of ~1.5 nm EELS measurements are performed in the scanning TEM mode with an energy resolution of 1.2 eV in high vacuum before and after the gas exposure. For details of the analysis of the Mn L edge, see supporting information. EDX line scans shown in the supporting information Figure S2 are performed in a Philips CM12 electron microscope at 120keV in the scanning TEM mode with a spatial resolution of ~10 nm and an energy resolution of 130eV.

Electrochemical cell within the ETEM: An electrochemical cell is realized within the ETEM sample chamber using a sample holder which includes a piezo-controlled STM Pt/Ir tip (Nanofactory). It allows for application of a bias voltage to the electron-transparent sample and to use the Pt/Ir tip in contact with specific sample areas as the counter electrode. Bias voltages between –1.5 V and +1.5 V applied to the TEM sample are suitable to control electrochemical reactions of a catalyst. The tip acting as a counter electrode remains grounded.

In-situ XANES measurements: The X-ray absorption spectra (XANES) were recorded using tunable monochromatic radiation from the ISISS (Innovative Station for In Situ Spectroscopy) beamline at the synchrotron radiation facility BESSY II (Berliner Elektronenspeicherringgesellschaft für Synchrotronstrahlung). The monochromator slit was set to 60 µm, corresponding to an energy resolution of about 0.2 eV. The spot size at the sample was 150 by 200 µm. Epitaxial PCMO thin film samples (x = 0.32) on Pt/MgO were positioned about 2 mm away from a 1 mm aperture, which is the entrance to the differentially-pumped electrostatic lens system separating gas molecules from photoelectrons focused toward the hemispherical analyzer (PHOIBOS 150, SPECS GmbH). The experimental setup is described in more detail elsewhere.[42] Experiments were performed in ultra high vacuum (UHV) and in H_2O vapor (flow of 3 ml/min. at 0.1 mbar). Sample 1 was put in to the UHV chamber without additional surface treatment and the Mn L core near edge features were measured in UHV and in H_2O vapor with an applied bias of +1.3 V. Sample 2 was treated ex-situ in H_2O (dest.) for 2 h. It was then exposed to Ar^+ sputtering in 1.3×10^{-4} mbar Ar for 12 min in the transfer chamber to remove surface carbon. After stabilization of H_2O pressure, an external bias of +1.3 and +1.8 V, respectively, was applied to the sample. The spectra presented here show the Auger electron yield (AEY). The intensities have been normalized with respect to the impinging photon flux.

Supporting Information

Supporting Information is available from the Wiley Online Library or from the author.

Acknowledgements

This research carried out in part at the Center for Functional Nanomaterials, Brookhaven National Laboratory, which is supported by the U.S. Department of Energy, Office of Basic Energy Sciences, under Contract No. DE-AC02-98CH10886. Research in Göttingen is supported by the DFG within the SFB 602. Financial support of the Research at TU Clausthal by the DFG through FOR 1346 is gratefully acknowledged. The XANES measurements performed at HZB/BESSY II (Helmholtz-Zentrum Berlin) were performed in collaboration with Rosita Arrigo and Axel Knop-Gericke from FHI (Fritz-Haber-Institute of the Max-Planck-Society Berlin). We gratefully acknowledge the Differential Mass Spectroscopy measurements and valuable discussion about electrochemistry with P. Bogdanoff and S. Fiechter, Institute of Solar Fuels, Helmholtz-Center for Materials and Energy, Berlin. Valuable discussions with M. Beleggia, Technical University of Denmark, Center for Electron Nanoscopy about electron-sample interactions are gratefully acknowledged.

Received: December 29, 2011
Revised: March 1, 2012
Published online: May 2, 2012

[1] L. I. Krishtalik, *Biochim. Biophys. Acta* **1986**, *849*, 162.
[2] K. N. Ferreira, T. M. Iverson, K. Maghlaoui, J. Barber, S. Iwata, *Science* **2004**, *303*, 1831.
[3] J. Barber, *Chem. Soc. Rev.* **2009**, *38*, 185.
[4] H. Dau, I. Zaharieva, *Acc. Chem. Res.* **2009**, *42*, 1861.
[5] J. Messinger, *Phys. Chem. Chem. Phys.* **2004**, *6*, 4764.
[6] J. P. McEcvoy, G. W. Brudvig, *Chem. Rev.* **2006**, *106*, 4455.
[7] F. A. Armstrong, *Phil. Trans. R. Soc. B* **2008**, *363*, 1263.
[8] G. F. Moore, G. W. Brudvig, *Ann. Rev. Condens. Matter Phys.* **2011**, *2*, 303.
[9] F. E. Osterloh, *Chem. Mater.* **2008**, *20*, 35.
[10] M. A. Pena, J. L. G. Fierro, *Chem. Rev.* **2001**, *101*, 1981.
[11] B. Viswanathan, Ch. Venkateswara Rao, U. V. Varadaraju, *Photo/Electrochem. Photobiol. Environ., Energy Fuel* **2006**, 43–101.
[12] J. O. Bockris, T. Otagawa, *J. Electrochem. Soc.* **1984**, *131*, 290.
[13] J. Rossmeisl, Z.-W. Qu, H. Zhu, G.-J. Kroes, J. K. Nørskov, *J Electroanal. Chem.* **2007**, *607*, 83.
[14] E. M. Fernandez, P. G. Moses, A. Toftelund, H. A. Hansen, J. I. Martinez, F. Abild-Pedersen, J. Kleis, B. Hinnemann, J. Rossmeisl, T. Bligaard, J. K. Nørskov, *Angew. Chem.* **2008**, *120*, 4761.
[15] I. C. Man, H. Su, F. Calle-Vallejo, H. A. Hansen, J. I. Martinez, N. G. Inoglu, J. Kitchin, T. F. Jaramillo, J. K. Nørskov, J. Rossmeisl, *Chem. Cat. Chem.* **2011**, *3*, 1159.
[16] A. Vojvodic and J. K. Nørskov, *Science* **2011**, *334*, 1355.
[17] J. Suntivich, K. J. May, H. A. Gasteiger, J. B. Goodenough, Y. Shao-Horn, *Science* **2011**, *334*, 1383.
[18] B. Raveau, *Phil. Trans. R. Soc. A* **2008**, *366*, 83.
[19] Y. Tokura, in *Colossal magnetoresistive oxides (Advances in Condensed Matter Science)* Vol. *2* (Gordon and Breach, Amsterdam, **2000**).
[20] S. Schramm, J. Hoffmann, C. Jooss, *J. Phys.: Condens. Matter* **2008**, *20*, 395231.
[21] C. Jooss, L. Wu, T. Beetz, R. F. Klie, M. Beleggia, M. A. Schofield, S. Schramm, J. Hoffmann, Y. Zhu, *Proc. Natl. Acad. Sci. USA* **2007**, *104*, 13597.
[22] L. Y. Chang, A. S. Barnard, L. C. Gontard, R. E. Dunin-Borkowski, *Nano Lett.* **2010**, *10*, 3073.
[23] T. W. Hansen, J. B. Wagner, R. E. Dunin-Borkowski, *Mater. Sci. Technol.* **2010**, *26*, 1338.
[24] E. D. Boyes, P. L. Gai, *Ultramicroscopy* **1997**, *67*, 219.
[25] P. L. Hansen, J. B. Wagner, S. Helveg, J. R. Rostrup-Nielsen, B. S. Clausen, H. Topsøe, *Science* **2002**, *295*, 2053.

[26] S. Helveg, C. López-Cartes, J. Sehested, P. L. Hansen, B. S. Clausen, J. R. Rostrup-Nielsen, F. Abild-Pedersen, J. K. Nørskov, *Nature* **2004**, *427*, 426.
[27] K. H. Downing, M. R. McCartney, R. M. Glaeser, *Microsc. Microanal.* **2004**, *10*, 783.
[28] J. H. Jung, K. H. Kim, D. J. Eom, T. W. Noh, E. J. Choi, J. Yu, Y. S. Kwon, Y. Chung, *Phys. Rev. B* **1997**, *55*, 15489.
[29] G. Zampieri, M. Abbate, F. Prado, A. Caneiro, E. Morikawa, *Physica B: Condens. Matter* **2002**, *320*, 51.
[30] J.-H. Park, C. T. Chen, S.-W. Cheong, W. Bao, G. Meigs, V. Chakarian, Y. U. Idzerda, *Phys. Rev. Lett.* **1996**, *76*, 4215.
[31] Y. S. Lee, T. Arima, S. Onoda, Y. Okimoto, Y. Tokunaga, R. Mathieu, X. Z. Yu, J. P. He, Y. Kaneko, Y. Matsui, N. Nagaosa, Y. Tokura, *Phys. Rev. B* **2007**, *75*, 144407.
[32] K. Ebata, M. Hashimoto, K. Tanaka, A. Fujimori, Y. Tomioka, Y. Tokura, *Phys. Rev. B* **2007**, *76*, 174418.
[33] J. Kotakoski, C. H. Jin, O. Lehtinen, K. Suenaga, A. V. Krasheninnikov, *Phys. Rev. B* **2010**, *82*, 113404.
[34] S. Raabe, M. Beleggia, J. Ciston, C. Jooss, unpublished.
[35] J. D. Ferguson, Y. Kim, L. Fitting Kourkoutis, A. Vodnick, A. R. Woll, D. A. Muller, J. D. Brock, *Adv. Mater.* **2011**, *23*, 1226.
[36] S. Bakardjieva, P. Bezdička, T. Grygar, P. Vorm, *J. Solid State Electrochem.* **2000**, *4*, 306.
[37] A. Nemudry, P. Rudolf, R. Schöllhorn, *Chem. Mater.* **1996**, *8*, 2232.
[38] E. Beyreuther, S. Grafström, L. M. Eng, Ch. Thiele, K. Dörr, *Phys. Rev. B* **2006**, *73*, 155425.
[39] T. Grygar, *J. Solid State Electrochem.* **1999**, *3*, 412.
[40] F. Calle-Vallejo, J. I. Martínez, J. M. García-Lastra, M. Mogensen, J. Rossmeisl, *Angew. Chem. Int. Ed.* **2010**, *49*, 7699.
[41] B. D. White, C. A. M. Dos Santos, J. A. Souza, K. J. McClellan, J. J. Neumeier, *J. Crystal Growth* **2008**, *310*, 3325.
[42] E. M. Vass, M. Hävecker, S. Zafeiratos, D. Teschner, A. Knop-Gericke, R. Schlögl, *J. Phys.: Condens. Matter* **2008**, *20*, 1.
[43] F. Ramezanipour, J. E. Greedan, J. Siewenie, Th. Proffen, D. Ryan, A. P. Grosvenor, R. L. Donaberger, *Inorg. Chem.* **2011**, *50*, 7779.